Compressed Sensing 3-Dimensional Time-of-Flight Magnetic Resonance Angiography for Cerebral Aneurysms: Optimization and Evaluation.

AUTHOR(S):

Fushimi, Yasutaka; Fujimoto, Koji; Okada, Tomohisa; Yamamoto, Akira; Tanaka, Toshiyuki; Kikuchi, Takayuki; Miyamoto, Susumu; Togashi, Kaori

CITATION:

Fushimi, Yasutaka ...[et al]. Compressed Sensing 3-Dimensional Time-of-Flight Magnetic Resonance Angiography for Cerebral Aneurysms: Optimization and Evaluation.. Investigative radiology 2016, 51(4): 228-235

ISSUE DATE:

2016-04

URL:

http://hdl.handle.net/2433/202829

Compressed Sensing 3D TOF-MRA for Cerebral Aneurysms: Optimization and Evaluation

ABSTRACT

Objectives: To optimize parameters for Nesterov's Algorithm (NESTA) in reconstruction of 3D time-of-flight Magnetic Resonance angiography (TOF-MRA) at 3 T by performing an exhaustive search and to validate the performance of CS by applying it to data from cerebral aneurysms and evaluating diagnostic quality.

Materials and Methods: Three-dimensional TOF-MRA was obtained using a 3T MR system with a 32-channel head coil for both healthy volunteers and 10 patients (11 aneurysms). No undersampling was applied for imaging parameters, including parallel imaging or other partial Fourier sampling. In the first step, the experimental setup was for healthy subjects, to optimize CS parameters of NESTA and the undersampling mask pattern, so 24,696 different reconstruction conditions were surveyed for sampling rates of 8.0X and 5.0X. Mean square error (MSE) was calculated for each image reconstructed with the undersampling pattern and CS parameter sets. Evaluation was by normalized MSE (NMSE), edge sharpness for MRA reconstructed using fully sampled data (MRA-full), zero-filled MRA (ZF-MRA) with Poisson disk undersampling mask, and CS-MRA (5.0X and 8.0X) with iterations of 5, 10, 15, 20, 25, 30, 35, 40, 45, and 50. CS-MRA (5.0X and 8.0X) with 5, 10, and 50 iterations of the sampling pattern and CS

parameter set with the lowest MSE were visually inspected by two neuroradiologists to check the diagnostic quality.

Results: The sampling pattern and CS parameter set with the lowest MSE were identical for both CS-MRA 5.0X and CS-MRA 8.0X. At the initial 5-15 iterations, MSE of both sampling rates greatly decreased from that of ZF-MRA. For subsequent iterations, the decrease in MSE was relatively small. For CS-MRA, sharpness greatly increased from that of ZF-MRA within the initial 5-15 iterations, followed by slight increases with further iterations. Two neuroradiologists graded most aneurysms as excellent, with the exception of 1-4 aneurysms recognized as good by one observer in CS-MRA (8.0X).

Conclusions: Optimization of NESTA in the reconstruction of 3D TOF-MRA was conducted and the parameters and undersampling mask with the lowest MSE were determined. Caliber measurement should be performed with CS (5.0X) with 25 or 30 iterations. Most cerebral aneurysms were sufficiently recognized using CS-MRA (5.0X) or CS-MRA (8.0X) with 10 iterations.

Key words: compressed sensing; time of flight MR angiography; NESTA; cerebral aneurysm; neuroradiology

INTRODUCTION

The application of compressed sensing (CS) on Magnetic Resonance (MR) provides an innovative approach to undersampling k-space by exploiting the underlying sparsity in the appropriate transform domain (e.g., wavelet transform), thereby reducing the number of samples required for reconstruction of MR data. This has been demonstrated in various MR applications, such as brain imaging, cardiac cine imaging,[1] dynamic contrast-enhanced imaging,[2-4] pediatric imaging including contrast-enhanced MR angiography (MRA),[5] parametric imaging, and MR spectroscopy.[6] Reports on these applications have not featured cerebral time-of-flight (TOF)-MRA, with the exception of a recent report on brain TOF-MRA for healthy volunteers obtained at 1.5 T.[7] TOF imaging allows for high spatial resolution, but is associated with limited anatomical coverage due to relatively long acquisition times.[8] TOF-MRA has been used in clinical settings at 3 T, and visualized more vessels at 3 T than at 1.5 T due to elongation of the T1 relaxation time and an increased magnetization transfer effect.[9]

Several algorithms are used for CS. Iterative Shrinkage Thresholding Algorithm (ISTA) and Fast ISTA (FISTA) are well-known operator-splitting algorithms,[10] but both ISTA and FISTA are designed for simpler regularization problems and cannot be applied efficiently to the composite regularization problem using both L1

norm and total variation (TV). Conversely, Nesterov's Algorithm (NESTA) [11] has been referred to as an algorithm offering desirable speed, accuracy, and flexibility.[12]

Since undersampling in CS may reduce the image quality of MR, the impairment of diagnostic quality should be minimized in applications of CS for clinical MR imaging. We therefore focused on the depiction of cerebral aneurysms in this study to evaluate benchmark tests of CS for cerebral MR angiography. Optimization of CS should be conducted to ensure the reconstructed images contain clinical diagnostic value, but clinical diagnosis-orientated optimization methods have not been established in CS MR for TOF-MRA. Un-ruptured cerebral aneurysm >7 mm is reportedly associated with an increased risk of rupture (1.69% per year for 7- to 9-mm diameter aneurysms).[13, 14] Conversely, the risk of rupture of a single aneurysm <5 mm in diameter is very low according to previous studies (0.34-0.36% per year).[13, 15] It is essential to maintain sufficient diagnostic quality to recognize cerebral aneurysms larger than 7 mm in the context of undesirable rupture of aneurysms for asymptomatic subjects.[16]

The purpose of this study was to optimize parameters for NESTA in the reconstruction of 3D TOF-MRA at 3 T by performing an exhaustive search and to validate the performance of CS by applying it to data from cerebral aneurysms and evaluating diagnostic quality.

MATERIALS AND METHODS

Written informed consent for a normal database of CS MR was obtained prospectively for four healthy volunteers, with protocols approved by the local institutional review board (IRB). The retrospective study for patients was likewise approved by the IRB and the need to obtain written informed consent was waived.

Imaging parameters

Three-dimensional TOF-MRA was obtained using a 3 T MR unit (Magnetom Trio; Siemens, Erlangen, Germany) with a 32-channel head coil for both healthy volunteers and patients: TR, 19 ms; TE, 3.69 ms; flip angle, 18°; field of view, 220 × 220 mm; matrix size, 384 × 384; in-plane resolution, 0.57 × 0.57 mm; and slice thickness, 0.57 mm. No undersampling was applied for the imaging parameter, including parallel imaging or other partial Fourier sampling. The k-space trajectory was acquired by linear Cartesian ordering. Total acquisition time was 12 min 30 s.

Experiment Setup

Image reconstruction with NESTA

CS reconstruction was conducted on an off-line PC workstation based on NESTA, modified and implemented to in-house script by Matlab 2013b (Mathworks, Natick, MA). [12] All parameters of NESTA were included in this script. NESTA solves the following problem:

$$\min_x \{\lambda_1 \|x\|_1 + \lambda_2 \|W(x)\|_1 + \lambda_3 \|TV(x)\|_1,\} \ s.t. \ \|y - Ax\|_2 \leq \varepsilon$$

where x is a reconstructed image, y denotes an observed data, and A represents a sampling matrix. The L1 norm of x, the L1 norm of wavelet transformation of x with Daubechies wavelet (W), and total variation of x (TV) were chosen as sparsity-inducing regularizers for CS reconstruction in this study. The parameters λ_1, λ_2, and λ_3 represent the regularization coefficients for these regularizers. The parameter ε defines the constraint on the L2 norm between the actually observed data y and its estimate Ax, on the basis of a tentative reconstruction x of the image. Specifying its value appropriately would require estimating measurement noise levels, but this would not be straightforward with most MR imaging, particularly in 3D TOF-MRA. NESTA has two parameters, μ and δ. The parameter μ specifies the degree of smoothness in approximating regularizers with smooth functions, and controls a trade-off between the accuracy of the approximations and the speed of convergence; that is, a small μ leads to high accuracy but slow convergence, while a large μ leads to fast convergence but low

accuracy. Our script adopted a double-loop structure, where the inner loop performs the NESTA algorithm with μ fixed, and the outer loop makes the value of μ smaller. The parameter δ specifies the stopping criterion of the algorithm. The stopping criteria δ was computed as follows: $\delta = \gamma^t \times \delta_0$, where t is the index of the outer loop, and δ_0 is the δ applied to the first outer loop. A fixed value of $\gamma = 0.1$ was used throughout in this study.

CS parameter sets

In the first step, raw data were Fourier-transformed in the readout dimension. Because no undersampling would be applicable in a readout dimension, CS reconstruction was designed to be performed for a stack of 2D slices.

The above procedure of CS image reconstruction uses 8 parameters in total: the 3 regularization parameters λ_1, λ_2, and λ_3, the error-tolerance parameter ε, and the NESTA parameters μ and δ, as well as the numbers of iterations in the inner and the outer loops. We call a set of values of these 8 parameters a CS parameter set. Several different CS parameter sets were exhaustively investigated to find the most appropriate CS parameter set for representative 2D slices of 4 healthy subjects. We considered four combinations of the regularization parameters, $[\lambda_1\text{-}\lambda_2,\text{-}\lambda_3]$ = [1-1-1, 1-0-0, 0-1-0, 0-0-1], and 7 values $[10^{-1}, 10^{-2}, 10^{-3}, 10^{-4}, 10^{-8}, 10^{-12}, 10^{-16}]$ for each of μ, ε, and δ, so that these parameters would range from sufficiently small to sufficiently large. The number of

iterations in the inner loop was fixed to 50. The number of iterations in the outer loop was set either 1 or 2. We therefore considered a total of 4 × 7 × 7 × 7 × 2 = 2,744 different CS parameter sets.

Undersampling patterns

Most CS MRI studies adopted k-space undersampling patterns, which acquire more samples with low frequencies and less samples with high frequencies.[1, 17, 18] However, few studies have compared different undersampling patterns in the k-space. The present study compared CS reconstructions obtained from different undersampling patterns to see what types of undersampling patterns would be suitable for the diagnosis of cerebral aneurysms. We prepared undersampling patterns as follows. First, we divided the whole k-space with two circles with different radii into three regions. Each region corresponds to the low-frequency, moderate-frequency, and high-frequency regions. The radius of the inner circle were also varied (small, radius = 48; medium, 60; and large, 72). Region within the inner circle (low-frequency region) was fully sampled. The ratio of the sampling density for the high-frequency region (region outside the outer circle) and the moderate-frequency region (region between the inner and outer circles) were defined in three different ways (i.e., 2:1, 1:1, 1:2). The actual sampling rate for the moderate and high frequency regions are defined so that the total sampling rate will achieve either

12.5% (acceleration factor of 8, 8.0X) or 20.0% (acceleration factor of 5, 5.0X). Consequently, 9 undersampling patterns were created and used for each of the acceleration factors 8.0X and 5.0X (Fig. 1).

Optimization process for undersampling pattern and CS parameter set

For each combination of a subject and an acceleration factor, 9 different undersampling patterns were applied to the original image, and 2,744 different CS parameter sets were tried for each undersampled data. In total, 2,744 × 9 = 24,696 different settings were surveyed. Mean square error (MSE) between the reconstructed image and the original image was evaluated for each setting, and the setting with the smallest MSE among the 2,744 settings was selected as the best CS parameter set for each combination of a subject, an acceleration factor, and an undersampling pattern.

Patients with cerebral aneurysms

A total of 11 cerebral aneurysms in 10 patients were included for analysis. CS reconstruction was performed in a retrospective manner. All the patients had already been diagnosed as cerebral aneurysms by contrast-enhanced computed tomography angiography or conventional angiography. No patients underwent surgery or intervention for aneurysms. Patient profiles and the locations of cerebral aneurysms are

listed in Table 1.

Evaluation by NMSE

Zero-filled MRA with Poisson disk undersampling mask (ZF-MRA) and CS-MRA for cerebral aneurysms with the best undersampling pattern and the best image reconstruction parameters were compared with MRA reconstructed using fully sampled data (MRA-full) by means of normalized MSE (NMSE) averaged over all slices. ZF-MRA and CS-MRA (5.0X and 8.0X) with iterations of 5, 10, 15, 20, 25, 30, 35, 40, 45, and 50 were compared with MRA-full.

Evaluation by edge sharpness

To elucidate the effect of CS reconstruction, sharpness at the aneurysm edge was calculated.[4, 19] Sharpness was defined as the distance between 20% and 80% of maximum signal intensity for the Gaussian fitted line profile of the aneurysm and neighboring structure, calculated using ImageJ software (http://imagej.nih.gov/ij/index.html). Edge sharpness was calculated for ZF-MRA and CS-MRA (5.0X and 8.0X) with iterations of 5, 10, 15, 20, 25, 30, 35, 40, 45, and 50 as well as MRA-full. In order to compensate for differences in aneurysm size among

patients, and differences in the signals of neighboring structures among aneurysms, measured edge sharpness for ZF-MRA and CS-MRA was normalized to that of MRA-full.

Evaluation by neuroradiologists

Three-dimensional CS-MRA (5.0X and 8.0X) with 5, 10, and 50 iterations of the best CS parameter set with the best sampling pattern were visually inspected by 2 neuroradiologists (_._, 18 years of experience and _._, 23 years of experience). They were blinded to the acceleration factor (5.0X, 8.0X) and iteration times (5, 10 and 50) of CS-MRA. The images were presented randomly. The grading of cerebral aneurysms was defined as follows: i) “excellent”, sufficiently recognized; ii) “good”, recognizable; and iii) “poor”, hard to recognize. The size, neck, height, and aspect ratio (height/neck) of aneurysms were measured by them.

RESULTS

Undersampling mask pattern

Parameters for the best undersampling pattern were identical for both CS-MRA 5.0X and CS-MRA 8.0X: the pattern with the diameter of 48 matrices (small) for the

fully sampled central low-frequency part, and the sampling density ratio between high-frequency and moderate-frequency of 2:1 (marked with the single star in Figure 1).

CS parameter set for NESTA algorithm

The best CS parameter set corresponding to the best sampling mask pattern was identical for both CS-MRA 5.0X and CS-MRA 8.0X: [μ, ε, δ] = [10^{-8}, 10^{-4}, 10^{-4} or 10^{-8} or 10^{-12} or 10^{-16}], [λ_1-λ_2-λ_3] = [0-1-0], iterations = 50, outer loop = 1. The value λ_2 is a weight for wavelet transformation as the sparse prior. The best CS parameter set corresponding to the undersampling pattern of each sampling density ratio between high- and moderate-frequency patterns is shown (see Table, Supplemental Digital Content 1). Representative images of CS-MRA are shown (see Figures, Supplemental Digital Content 2A, 2B, 3A, and 3B, which are created from the best CS parameter set corresponding to the undersampling pattern of each sampling density ratio between high- and moderate-frequency patterns).

Evaluation by NMSE

For all cases of cerebral aneurysm, MSE for ZF-MRA, CS-MRA reconstructed with the best undersampling pattern and best image reconstruction parameters, and

MRA-full were compared. The average of MSE for all patient data is shown in Figure 2. MSE of ZF-MRA and CS-MRA with sampling rate (8.0X) was larger than MSE of (5.0X) for those. At the initial 5-15 iterations, MSE of both sampling rates greatly decreased from that of ZF-MRA. For subsequent iterations, decreases in MSE were relatively small. Representative cases with each iteration are shown in Figure 3.

Evaluation by edge sharpness

Edge sharpness was calculated at the site of cerebral aneurysm (Fig. 4). Sharpness of the edge of the aneurysm for sampling rate (5.0X) was larger than that for (8.0X). Sharpness of ZF-MRA was the lowest in both sampling rates. For CS-MRA, sharpness greatly increased from that of ZF-MRA within the initial 5-15 iterations, followed by a slight increase with further iterations. The sharpness of CS-MRA (5.0X) at 35-50 iterations surpassed that of the 100% sampling rate MRA.

Evaluation by neuroradiologists

The two neuroradiologists graded most aneurysms as excellent (Figure 5). All aneurysms were recognized as excellent in CS-MRA (5.0X). In CS-MRA (5.0X), all aneurysms were recognized as excellent by both neuroradiologists, and in CS-MRA

(8.0X), 63.6%, 90.9% and 90.9% of aneurysms were recongnized as excellent by both neuroradiologists. Inter-rater agreement (kappa) was 1 for CS-MRA (5.0X, 5, 10, and 50 iterations), and 0.143 for CS-MRA (8.0X, 5, 10, and 50 iterations). Representative cases for each iteration are shown in Figures 6 and 7. The measured size, neck, height, and aspect ration of aneurysms in CS-MRA are shown (see Tables, Supplemental Digital Content 4A, 4B, 4C, 4D, 4E, and 4F). The intraclass correlation coefficient between observer 1 and observer 2 were calculated (see Table, Supplemental Digital Content 5).

DISCUSSION

An exhaustive search for CS-MRA was successfully conducted and the best CS parameter set corresponding to the best sampling mask pattern was determined in this study. Sampling patterns with the smallest diameter (48) for a fully sampled central circle, and a sampling density ratio of 1:2 between high and moderate frequency were chosen as the best sampling mask pattern for both 8.0X and 5.0X in this study. Under the fixed sampling rate, a larger central circle led to a smaller sampling density around the high- and moderate-frequency parts. The selected sampling pattern showed a tendency for gradual transition from the central lower-frequency to the peripheral

higher-frequency part, consistent with the sampling mask reported in previous investigations.[5] A more gradual transitional sampling pattern can be achieved with a much smaller diameter of the central lower-frequency part, but the accuracy of coil sensitivity map estimation will be hampered.

NESTA was successfully applied for TOF-MRA in this study. MSE with the MRA-full decreases with iteration in the most optimized CS parameter set. While a smaller MSE can be achieved with more iteration, it takes more reconstruction time. Little visual change in reconstructed images was seen after 30 iterations. CS-MRA of 10 iterations provided adequate image quality for the clinical diagnosis of cerebral aneurysms, and stopping criteria for iterations can be verified with fewer iterations (Fig. 3). Accurate measurement of aneurysms is dependent on the accuracy of the edge sharpness of aneurysms. In this regard, CS-MRA (5.0X) with 25 or 30 iterations appears satisfactory for measurement of aneurysms (Fig. 4).

An exhaustive search of the CS framework was performed for NESTA. There are many parameters for CS reconstruction in NESTA, so there is no integrated optimization process in NESTA. In our exhaustive search, parameters for the best undersampling pattern as well as the best CS parameter set corresponding to the best undersampling pattern were identical among four healthy volunteers. These consistent

results also supported validity of our optimization process. MRA-full can be assumed as the reference standard, and the lowest NMSE represents the most nearest image to the reference standard. No established optimization has been reported, but our results suggest that chosen parameters can be applied for CS-MRA.

Several limitations must be considered in this study. ZF-MRA, as the zero-fill random undersampling, was designated as the initial image of CS reconstruction in this study. Other 'initial' images of CS reconstruction are possible, such as the zero-filled reconstructed image after density compensation function. [1, 20] However, we chose to start the iteration from the blurry zero-filled image in order to easily evaluate the increase in the edge sharpness. Another limitation is that cerebral aneurysms are commonly located at branch points of the proximal intracranial cerebral artery. Arterial disease of peripheral portions was not evaluated in this study. Sensitivity and specificity were not evaluated in this study. CS-MRA for patients with cerebral aneurysms and more healthy volunteers will be conducted for sensitivity and specificity analyses. CS reconstruction was performed in a retrospective manner in this study. When CS sequence is scanned prospectively, there will be artifacts such as eddy current artifacts, phase artifacts and mapping of the sampling mask to the gradient hardware constraints of slew rate and maximum gradient strength during acquisition of pseudo-random data.

Moreover, the sampling pattern should typically incorporate these criteria in addition to the transform point spread function analyses.

The freely available software for optimal tuned implementations for CS was not used in this study. [21] It is obviously important to compare NESTA algorithms with other CS algorithms by using open source code for reproducible researches. However, noise has not been considered in their extensive computational experiments, therefore, their results cannot be applied to our data. Moreover, Iterative Soft Thresholding (IST) and Iterative Hard Thresholding (IHT) are usually used for solving quadratic programming (QP). Instead, NESTA solves basis pursuit, therefore, it is difficult to apply the results of their software to our NESTA scripts. Khare K, et al. reported a method to determine a threshold value for the IST in a data-driven manner, and compared it with the conventional nonlinear conjugate gradient (NLCG) method.[22] In the paper, a metric called Stein's Unbiased Risk Estimate (SURE) was used to determine a threshold value for IST by a data-driven manner, while NLCG required manual tuning for each data set. Our tuned data optimized by the exhaustive search might be compared with IST with SURE. IST with SURE was successful in determining a parameter for the threshold, but it is not clear that this method is useful for determining optimal combination of multiple parameters investigated in this study. [22]

L-curve analysis for multiple regularization parameters might be considered in this study.[23] However, L-curve method was generally used for quadratic programming (QP) for determination of the balance between data consistency term and sparse prior term. Since NESTA solves for a basis pursuit (BP) problem, L-curve method was not applicable to our data. Fractional weights were not used for three λs for sparse priors in this study, which is another limitation. Because far larger number of settings of undersampling pattern and CS parameter set were expected, four fixed weights were adopted in this study, and the most optimized combination was $[\lambda_1\text{-}\lambda_2,\text{-}\lambda_3]$ = [0-1-0], i.e., Daubechies wavelet, for both 8.0X and 5.0X. More efficient way of fractional weights for exhaustive searches should be established in future studies.

The sampling patterns used in this study were similar to that used in time-resolved angiography with stochastic trajectories (TWIST)[24] or DIfferential Sub-sampling with Cartesian Ordering (DISCO)[25], which are used in k-t direction for k-space sharing in dynamic contrast study. The characteristic of this study was that we have examined sampling patterns with higher sampling density on the high-frequency regions, which previously have never been performed. The point spread functions among these different sampling patterns were, however, very similar.

In conclusion, optimization of parameters for NESTA in the reconstruction of

3D TOF-MRA was conducted. The parameters and undersampling mask have been determined. Caliber measurement should be performed with CS (5.0X) with 25 or 30 iterations. Most cerebral aneurysms were sufficiently recognized in CS-MRA (5.0X) and CS-MRA (8.0X) with 10 iterations.

REFERENCES

1. Lustig M, Donoho D, Pauly JM. Sparse MRI: The application of compressed sensing for rapid MR imaging. *Magn Reson Med*. 2007;58:1182-1195.

2. Jung H, Sung K, Nayak KS, et al. k-t FOCUSS: a general compressed sensing framework for high resolution dynamic MRI. *Magn Reson Med*. 2009;61:103-116.

3. Chandarana H, Block TK, Ream J, et al. Estimating liver perfusion from free-breathing continuously acquired dynamic gadolinium-ethoxybenzyl-diethylenetriamine pentaacetic acid-enhanced acquisition with compressed sensing reconstruction. *Invest Radiol*. 2015;50:88-94.

4. Stalder AF, Schmidt M, Quick HH, et al. Highly undersampled contrast-enhanced MRA with iterative reconstruction: Integration in a clinical setting. *Magn Reson Med*. 2014.

5. Vasanawala SS, Alley MT, Hargreaves BA, et al. Improved pediatric MR imaging with compressed sensing. *Radiology*. 2010;256:607-616.

6. Geethanath S, Baek HM, Ganji SK, et al. Compressive sensing could accelerate 1H MR metabolic imaging in the clinic. *Radiology*. 2012;262:985-994.

7. Konar AS, Aiholli S, Shashikala HC, et al. Application of Region of Interest Compressed Sensing to accelerate magnetic resonance angiography. *Conf Proc IEEE*

Eng Med Biol Soc. 2014;2014:2428-2431.

8. Patel MR, Klufas RA, Kim D, et al. MR angiography of the carotid bifurcation: artifacts and limitations. *AJR Am J Roentgenol*. 1994;162:1431-1437.

9. Fushimi Y, Miki Y, Kikuta K, et al. Comparison of 3.0- and 1.5-T three-dimensional time-of-flight MR angiography in moyamoya disease: preliminary experience. *Radiology*. 2006;239:232-237.

10. Beck A, Teboulle M. A fast iterative shrinkage-thresholding algorithm for linear inverse problems. *SIAM Journal on Imaging Sciences*. 2009;2:183-202.

11. Nesterov Y. Smooth minimization of non-smooth functions. *Mathematical programming*. 2005;103:127-152.

12. Becker S, Bobin J, Candès EJ. NESTA: a fast and accurate first-order method for sparse recovery. *SIAM Journal on Imaging Sciences*. 2011;4:1-39.

13. Investigators UJ, Morita A, Kirino T, et al. The natural course of unruptured cerebral aneurysms in a Japanese cohort. *N Engl J Med*. 2012;366:2474-2482.

14. Tominari S, Morita A, Ishibashi T, et al. Prediction model for 3-year rupture risk of unruptured cerebral aneurysms in Japanese patients. *Ann Neurol*. 2015;77:1050-1059.

15. Sonobe M, Yamazaki T, Yonekura M, Kikuchi H. Small unruptured intracranial

aneurysm verification study: SUAVe study, Japan. *Stroke*. 2010;41:1969-1977.

16. Wiebers DO, Whisnant JP, Huston J, 3rd, et al. Unruptured intracranial aneurysms: natural history, clinical outcome, and risks of surgical and endovascular treatment. *Lancet*. 2003;362:103-110.

17. Ma S, Yin W, Zhang Y, Chakraborty A. An efficient algorithm for compressed MR imaging using total variation and wavelets. Computer Vision and Pattern Recognition, 2008. CVPR 2008. IEEE Conference on, 2008. IEEE: 1-8.

18. Yang J, Zhang Y, Yin W. A fast alternating direction method for TVL1-L2 signal reconstruction from partial Fourier data. *Selected Topics in Signal Processing, IEEE Journal of*. 2010;4:288-297.

19. Kramer JH, Arnoldi E, Francois CJ, et al. Dynamic and static magnetic resonance angiography of the supra-aortic vessels at 3.0 T: intraindividual comparison of gadobutrol, gadobenate dimeglumine, and gadoterate meglumine at equimolar dose. *Invest Radiol*. 2013;48:121-128.

20. Pruessmann KP, Weiger M, Bornert P, Boesiger P. Advances in sensitivity encoding with arbitrary k-space trajectories. *Magn Reson Med*. 2001;46:638-651.

21. Maleki A, Donoho DL. Optimally tuned iterative reconstruction algorithms for compressed sensing. *Selected Topics in Signal Processing, IEEE Journal of*.

2010;4:330-341.

22. Khare K, Hardy CJ, King KF, et al. Accelerated MR imaging using compressive sensing with no free parameters. *Magn Reson Med*. 2012;68:1450-1457.

23. Belge M, Kilmer ME, Miller EL. Efficient determination of multiple regularization parameters in a generalized L-curve framework. *Inverse Problems*. 2002;18:1161.

24. Song T, Laine AF, Chen Q, et al. Optimal k-space sampling for dynamic contrast-enhanced MRI with an application to MR renography. *Magn Reson Med*. 2009;61:1242-1248.

25. Saranathan M, Rettmann DW, Hargreaves BA, et al. DIfferential Subsampling with Cartesian Ordering (DISCO): a high spatio-temporal resolution Dixon imaging sequence for multiphasic contrast enhanced abdominal imaging. *J Magn Reson Imaging*. 2012;35:1484-1492.

FIGURE LEGENDS

Figure 1

Sampling mask pattern used in this study. Nine different masks for k-space were created by Poisson disk sampling pattern, as follows: diameter of fully sampled central circle, [small 48 matrices, medium 60, large 72]; sampling density ratio between high and moderate frequency, 2:1, 1:1, and 1:2. Nine sampling mask patterns of 12.5% sampling rate (8.0X) are shown in the left column, and those of 20.0% sampling rate (5.0X) are shown in the right column. The best achievable MSE is shown on the upper right of each sampling mask. The mask pattern marked with the single star was chosen as the best sampling mask (sampling density ratio, 1:2). The best mask pattern among sampling masks with the other sampling density ratios was marked with 2 and 3 stars. MSE of the sampling mask with 2 stars is smaller than that with 3 stars.

Figure 2

ZF-MRA and CS-MRA for cerebral aneurysms with the best undersampling pattern and the best CS parameter sets were compared with 100% sampling rate MRA images by NMSE. Averaged NMSE for all patients' data is shown. NMSE of sampling rate (8.0X) was larger than NMSE of (5.0X). NMSE of both sampling rates greatly decreases from

ZF-MRA to CS-MRA with 5-15 iterations, whereas NMSE slightly decreases among CS-MRA with further iterations. Error bar represents the standard error of NMSE for all patients' data.

Figure 3

Maximum intensity projection (MIP) images of 3D TOF-MRA with a cerebral aneurysm (arrow) of the right ICA and a small aneurysm (arrowhead) of the left ICA. The top and second rows represent CS-MRA images created from a sampling rate of (8.0X), except the image of 100% sampling rate (1.0X or MRA-full) and ZF-MRA at left in the first row. The third and bottom rows represent CS-MRA images created from a sampling rate of (5.0X), except the image of MRA-full and ZF-MRA at left in the third row. The number of iterations in CS reconstruction is shown at the right upper corner of the image. CS-MRA (5.0X) with 5 iteration shows a ghost artifact associated with undersampling. However, CS-MRA (5.0X) with more than 10 iteration show reduced ghost artifacts. No changes are apparent between 15 and 50 iteration at both CS (5.0X) and CS (8.0X).

Figure 4

Average edge sharpness of all cerebral aneurysms is shown. Edge sharpness of the following images were calculated: ZF-MRA and CS-MRA (5.0X and 8.0X) of the best undersampling pattern and the best CS parameter sets with iterations of 5, 10, 15, 20, 25, 30, 35, 40, 45, and 50, as well as the 100% sampling rate MRA. Each edge sharpness of ZF-MRA and CS-MRA was normalized to that of the 100% sampling rate MRA (1.0X or MRA-full). Sharpness was larger for sampling rate (5.0X) than for (8.0X). Sharpness of ZF-MRA was lowest at both sampling rates. Sharpness of both sampling rates greatly increases from ZF-MRA to CS-MRA within 5-15 iterations; on the other hand, sharpness slightly increases among CS-MRA with more iterations. Note that sharpness of CS-MRA (5.0X) eventually surpassed that of 100% sampling rate MRA. Error bar represents the standard error. Accurate measurement of an aneurysm is dependent on the accuracy of edge sharpness of the aneurysm. In this regard, CS-MRA (5.0X) with more than 25 iteration times is satisfactory for measurement of aneurysms.

Figure 5

CS-MRA (5.0X and 8.0X) with 5, 10 or 50 iterations were visually inspected by two neuroradiologists. Cerebral aneurysms were graded as: i) “excellent”, sufficiently recognizable; ii) “good”, recognizable; and iii) “poor”, hard to recognize. Two

neuroradiologists graded most aneurysms as excellent. All aneurysms were recognized as excellent on CS-MRA (5.0X). All aneurysms were recognized as excellent, with the exception of 1-4 aneurysms recognized as good by one observer in CS-MRA (8.0X).

Figure 6

Source images (A) and maximum intensity projection (MIP) images (B) of 3D TOF-MRA for a 62-year-old man with aneurysm at the anterior communicating artery (arrow) (Case 8). Images of the upper row are created from mask patterns with a 12.5% sampling rate (8.0X) with the best optimized sampling mask, and those of the lower rows are from a 20.0% sampling rate (5.0X) with the best optimized sampling mask. Images in the left column represent identical MRA created from 100% sampling rate (1.0X or MRA-full). Images from the second left column are ZF-MRA, and images in the middle to right columns are CS-MRA with 5, 10, and 50 iterations. Note that no manual cut of skull or subcutaneous fat was applied to MIP data.

Figure 7

Source images (A) and maximum intensity projection (MIP) images (B) of a 68-year-old woman with right middle cerebral artery aneurysm (Case 10). Images of the

upper row are created from mask patterns with a 12.5% sampling rate (8.0X) with the best optimized sampling mask, and those of the lower rows are from a 20.0% sampling rate (5.0X) with the best sampling mask. Images in the left column represent identical MRA created from a 100% sampling rate (1.0X or MRA-full). Images in the second left column are ZF-MRA, and images in the middle to right columns are CS-MRA with 5, 10, and 50 iterations. Note that no manual cut of skull or subcutaneous fat was applied to MIP data.

Table 1. Location and diameter of cerebral aneurysms.

	Age	Sex	Location	Diameter (mm)
Case 1	35	F	Right ICA	5.0
Case 1			Left ICA	2.0
Case 2	64	F	BA	8.5
Case 3	62	F	Right MCA	6.5
Case 4	56	F	Left ICA	5.5
Case 5	44	M	Left ICA	8.0
Case 6	65	F	Left ICA	6.0
Case 7	65	F	Left ICA	3.0
Case 8	62	M	Acom	5.0
Case 9	76	F	Acom	6.0
Case 10	68	F	Right MCA	5.0

Note that two cerebral aneurysms were found in Case 1.

ICA: internal carotid artery, IC-PC: internal carotid–posterior communicating artery, Acom: anterior communicating artery, BA: basilar artery,

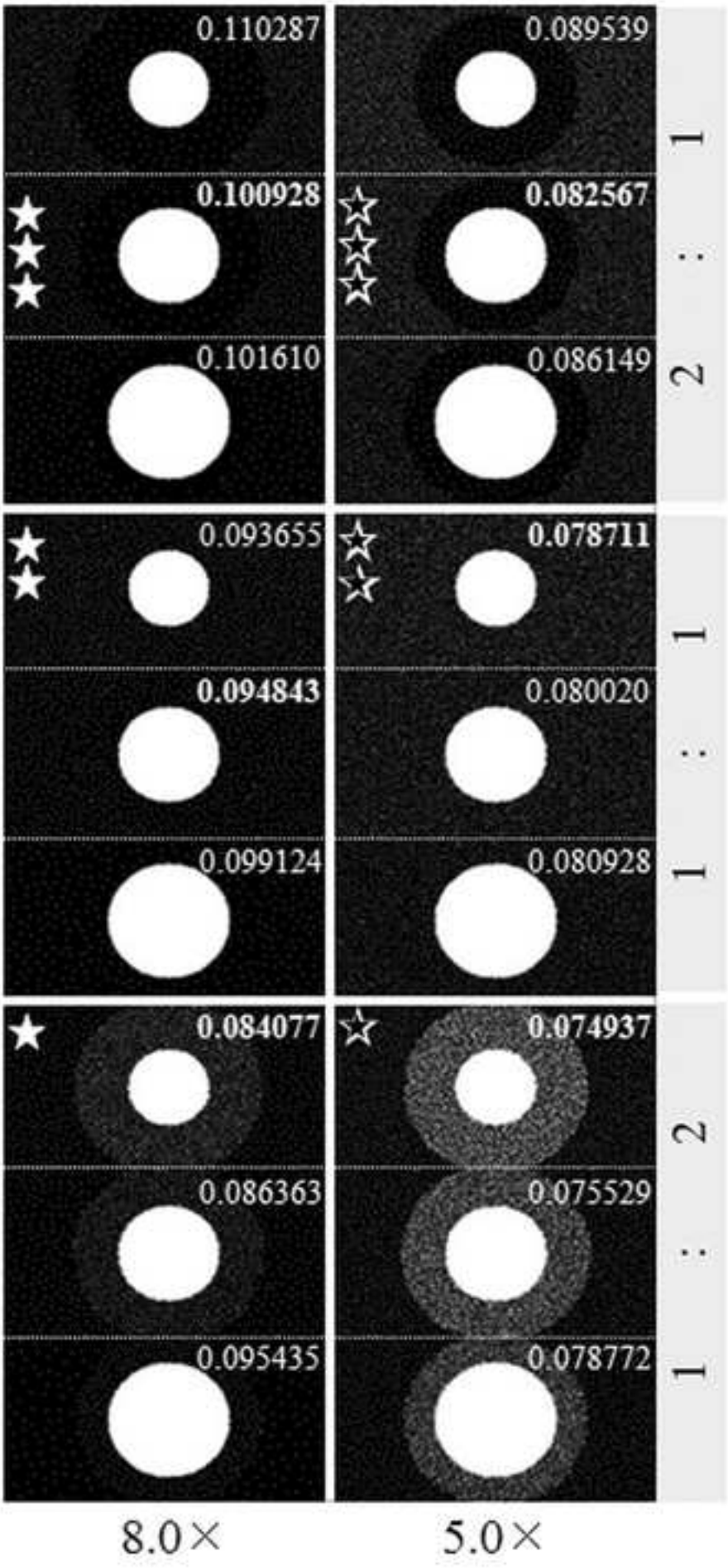

Figure 2

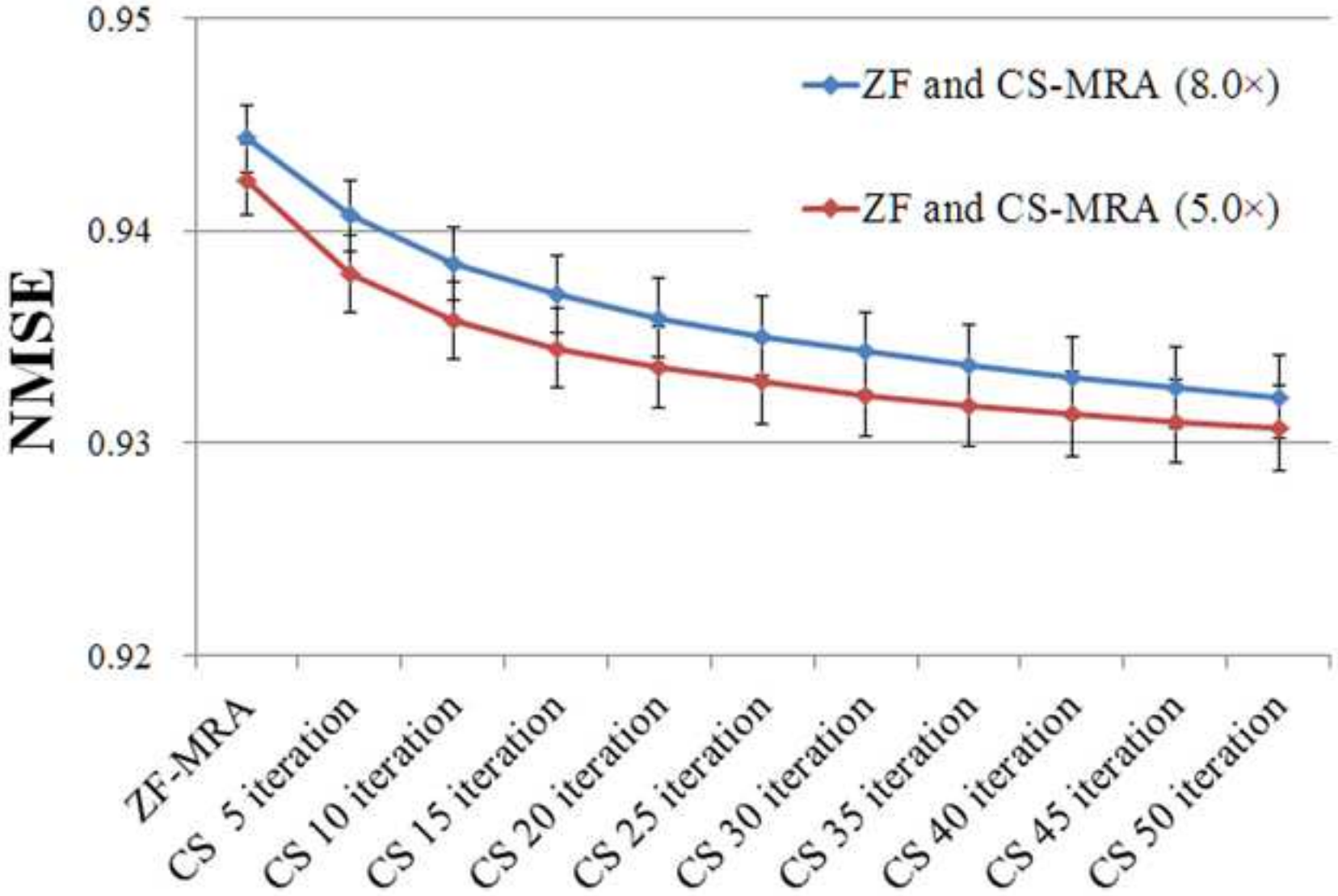
0.95
0.94
0.93
0.92
NMISE
ZF and CS-MRA (8.0×)
ZF and CS-MRA (5.0×)
ZF-MRA
CS 5 iteration
CS 10 iteration
CS 15 iteration
CS 20 iteration
CS 25 iteration
CS 30 iteration
CS 35 iteration
CS 40 iteration
CS 45 iteration
CS 50 iteration

Figure 3

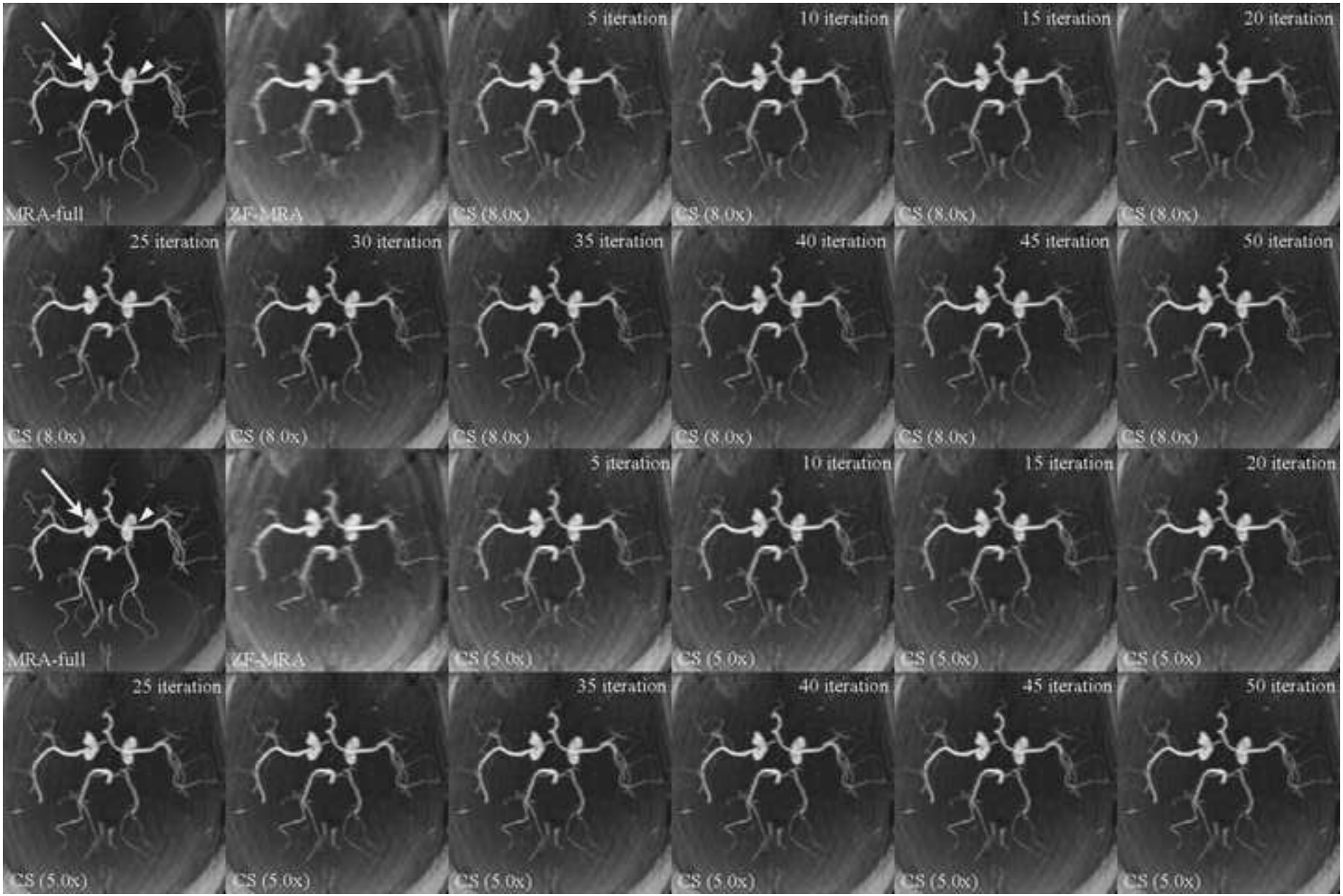
MRA-full
ZF-MRA
5 iteration
10 iteration
15 iteration
20 iteration
CS (8.0x)
25 iteration
30 iteration
35 iteration
40 iteration
45 iteration
50 iteration
MRA-full
ZF-MRA
5 iteration
10 iteration
15 iteration
20 iteration
CS (5.0x)
25 iteration
35 iteration
40 iteration
45 iteration
50 iteration
CS (5.0x)

Figure 4

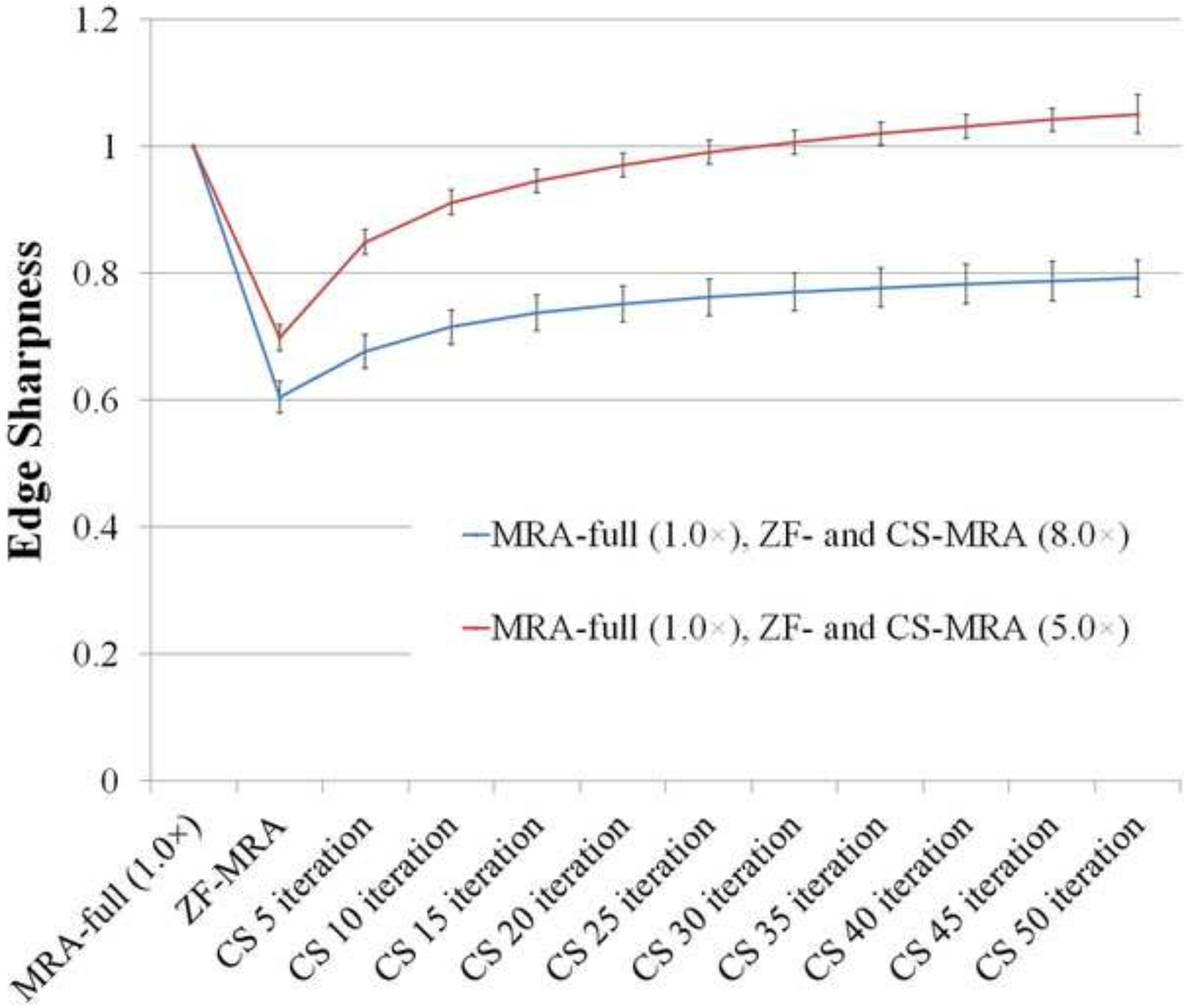
Edge Sharpness
1.2
1
0.8
0.6
0.4
0.2
0
MRA-full (1.0×), ZF- and CS-MRA (8.0×)
MRA-full (1.0×), ZF- and CS-MRA (5.0×)
MRA-full (1.0×)
ZF-MRA
CS 5 iteration
CS 10 iteration
CS 15 iteration
CS 20 iteration
CS 25 iteration
CS 30 iteration
CS 35 iteration
CS 40 iteration
CS 45 iteration
CS 50 iteration

Figure 5

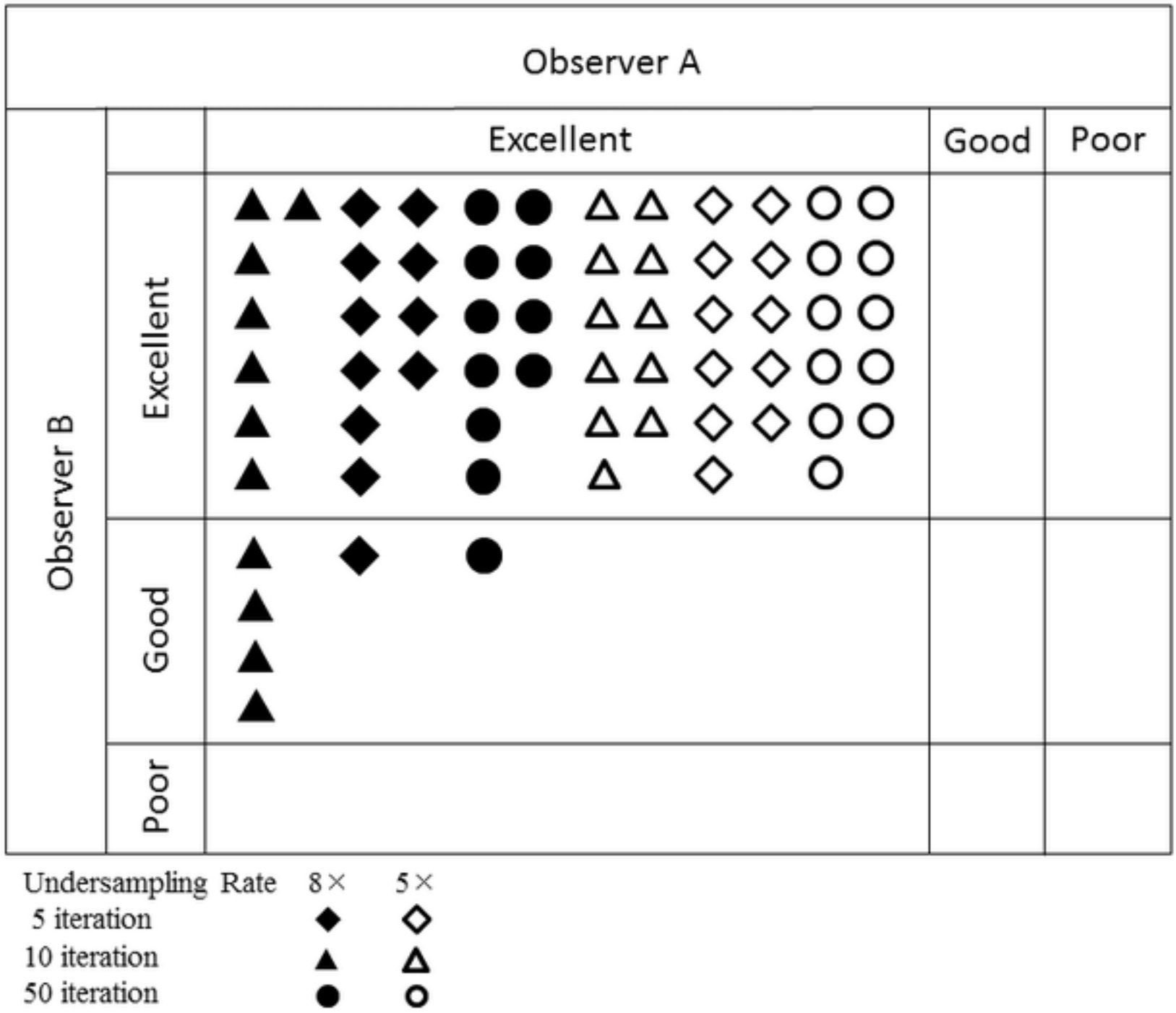
Observer A
Observer B
Excellent
Good
Poor
Excellent
Good
Poor
Undersampling Rate 8× 5×
5 iteration
10 iteration
50 iteration

Figure 6af

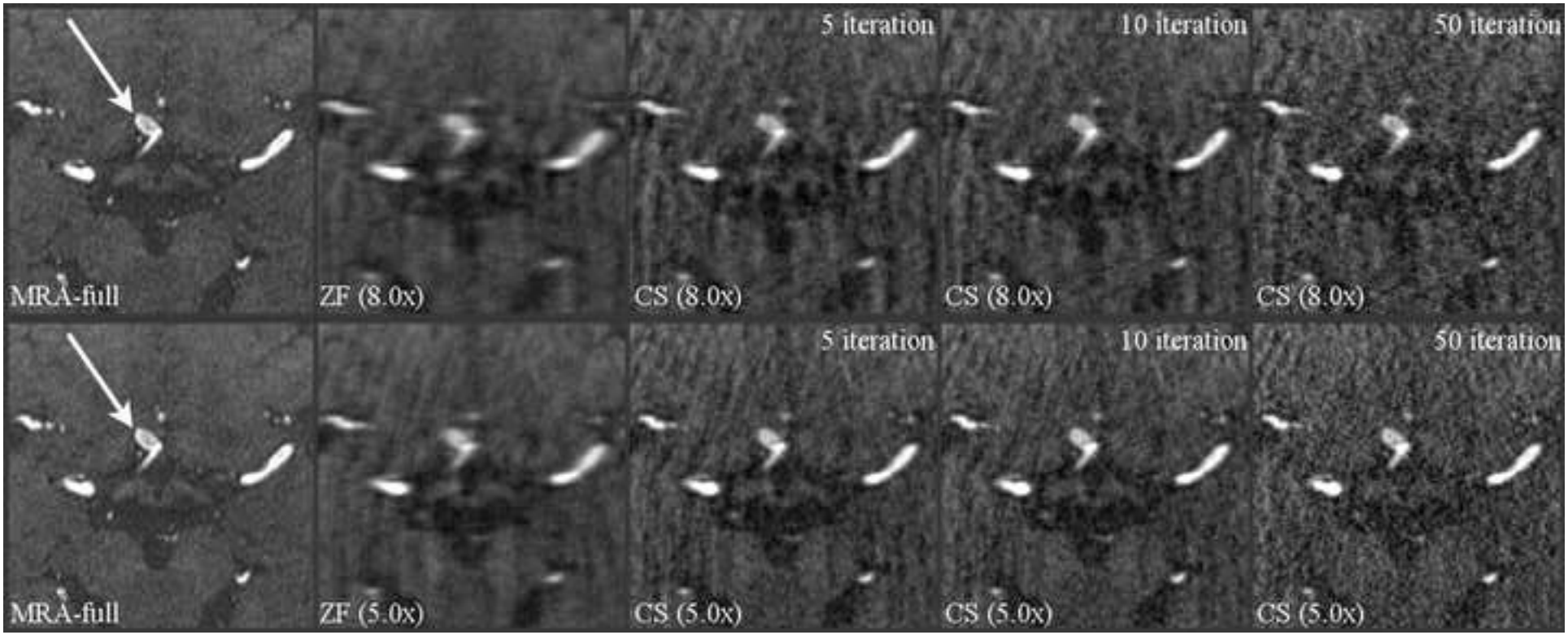
5 iteration
10 iteration
50 iteration
MRA-full
ZF (8.0x)
CS (8.0x)
CS (8.0x)
CS (8.0x)
5 iteration
10 iteration
50 iteration
MRA-full
ZF (5.0x)
CS (5.0x)
CS (5.0x)
CS (5.0x)

Figure 6b

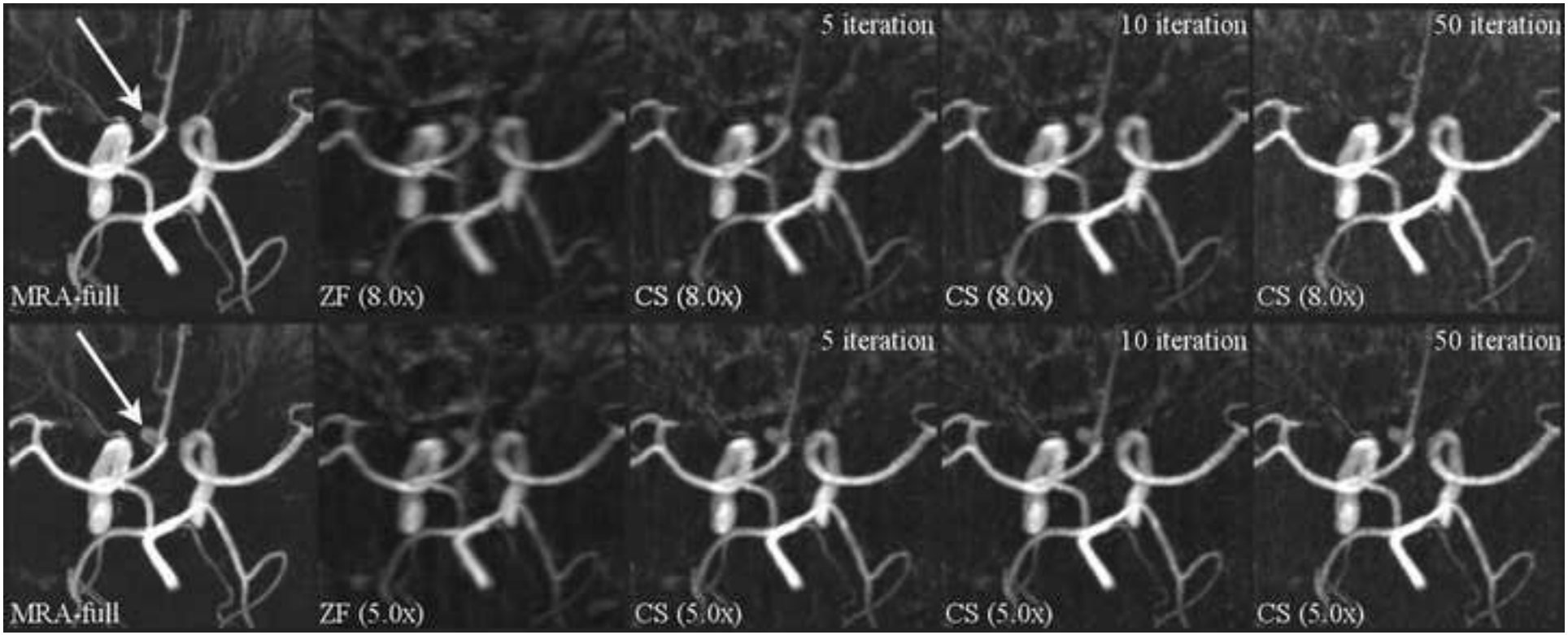
MRA-full
ZF (8.0x)
5 iteration
CS (8.0x)
10 iteration
CS (8.0x)
50 iteration
CS (8.0x)
MRA-full
ZF (5.0x)
5 iteration
CS (5.0x)
10 iteration
CS (5.0x)
50 iteration
CS (5.0x)

Figure 7a

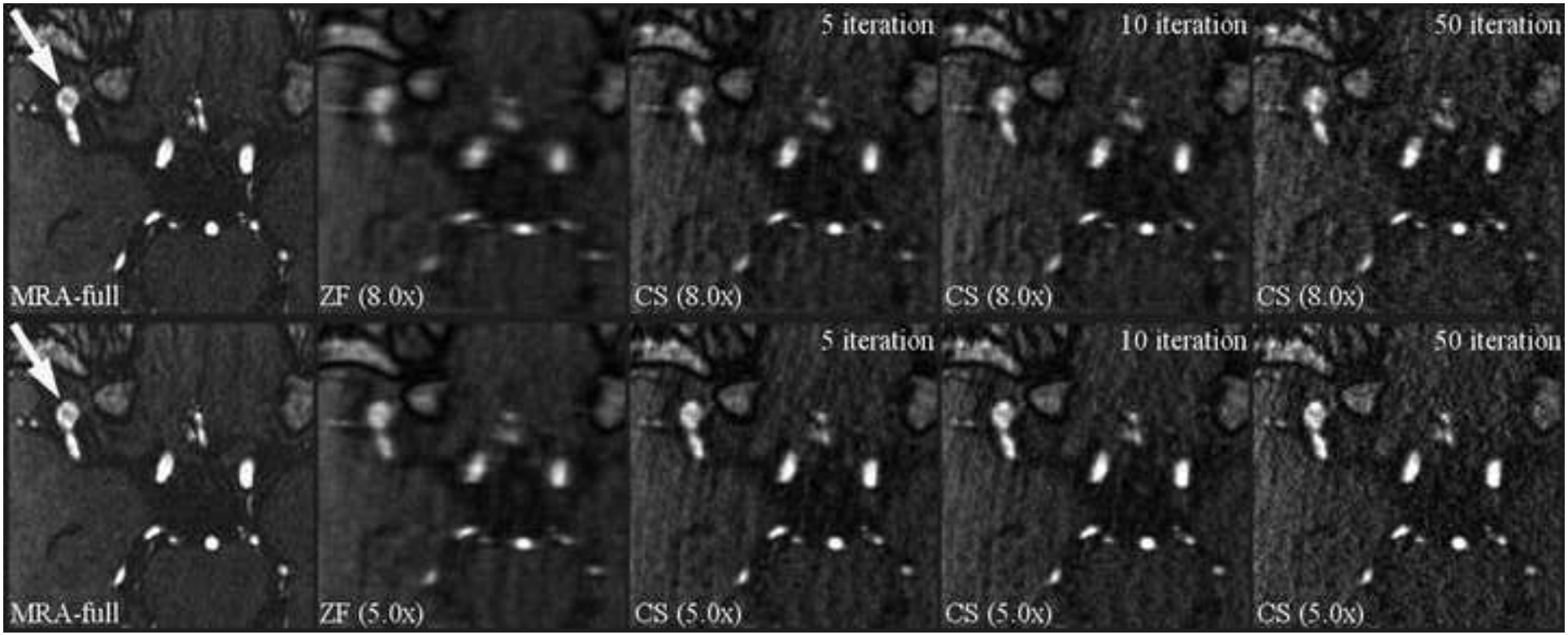
5 iteration
10 iteration
50 iteration
MRA-full
ZF (8.0x)
CS (8.0x)
CS (8.0x)
CS (8.0x)
5 iteration
10 iteration
50 iteration
MRA-full
ZF (5.0x)
CS (5.0x)
CS (5.0x)
CS (5.0x)

Figure 7b

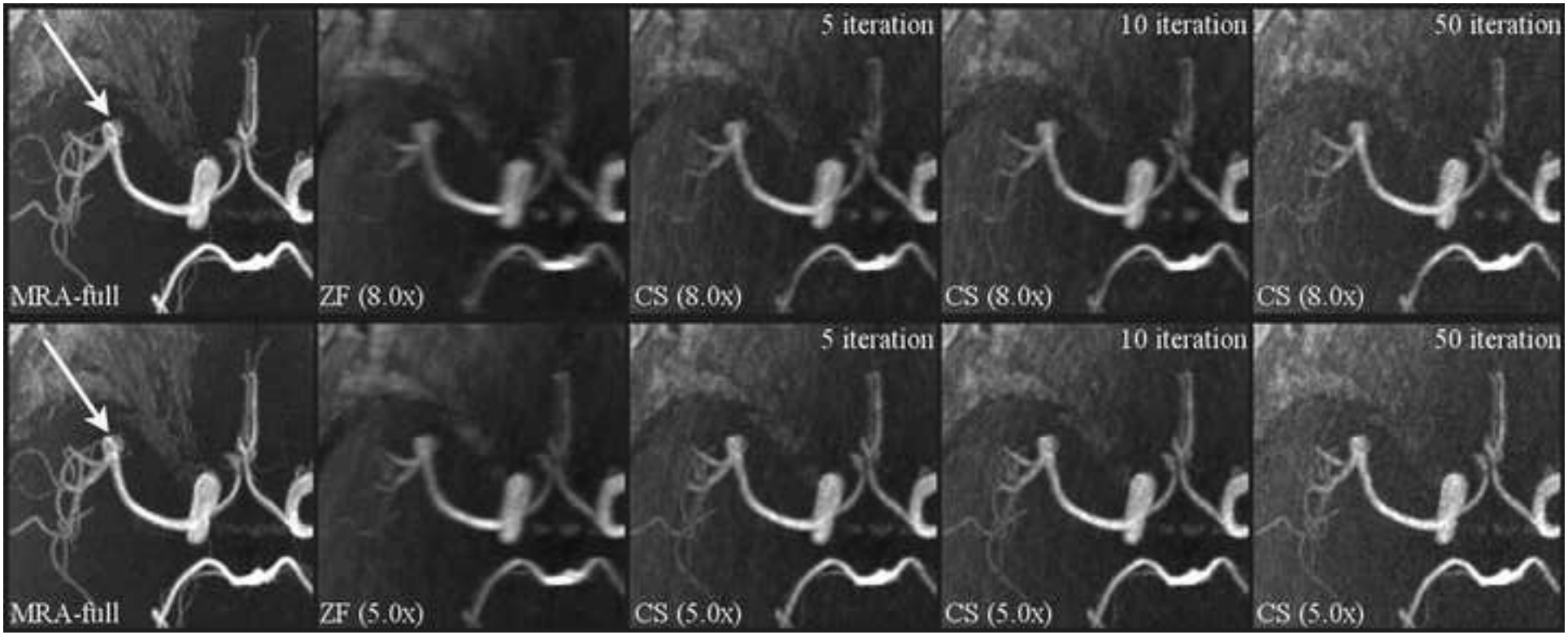
MRA-full
ZF (8.0x)
5 iteration
CS (8.0x)
10 iteration
CS (8.0x)
50 iteration
CS (8.0x)
MRA-full
ZF (5.0x)
5 iteration
CS (5.0x)
10 iteration
CS (5.0x)
50 iteration
CS (5.0x)

Supplemental Digital Content 1

The best CS parameter set corresponding to the undersampling pattern of each sampling density ratio between high- and moderate-frequency patterns is shown.

Supplemental Digital Content 2

Source images (A) and maximum intensity projection (MIP) images (B) of 3D TOF-MRA for a 62-year-old man with aneurysm at the anterior communicating artery (arrow) (Case 8). The best CS parameter set corresponding to the sampling mask pattern of each sampling density is shown in the Table, Supplemental Digital Content 1. CS-MRA from sampling mask patterns of each sampling density are shown. The best CS parameter sets for each sampling mask were used. Images in the upper 3 rows were created from mask patterns with a 12.5% sampling rate (8.0X), and those of the lower 3 rows with a 20.0% sampling rate (5.0X). The top of the upper 3 and lower 3 rows are images created from a sampling mask with sampling density ratio between high frequency and moderate frequency of 2:1; middle rows, 1:1; and bottom rows, 1:2, with ratio noted in the right upper corner of each image. Images in the left column are identical MRA created from a 100% sampling rate (1.0X or MRA-full). Images in the second left column are ZF-MRA, and images in the middle to the right columns are

CS-MRA with 5, 10 or 50 iterations, respectively. The best optimized CS parameter set for each sampling density led to images nearly equal to the chosen image.

Supplemental Digital Content 3

Source images (A) and maximum intensity projection (MIP) images (B) of a 68-year-old woman with right middle cerebral artery aneurysm (arrow) (Case 10).

The best CS parameter set corresponding to the sampling mask pattern of each sampling density is shown in the Table, Supplemental Digital Content 1. CS-MRA images from sampling mask patterns of each sampling density are shown. The best CS parameter sets for each sampling mask were used. Images of the upper 3 rows are created with mask patterns from a 12.5% sampling rate (8.0X), and those of the lower 3 rows are from a 20.0% sampling rate (5.0X). The top of the upper 3 rows and lower 3 rows are images created from the sampling mask with sampling density ratio between high and moderate frequency of 2:1; middle rows, 1:1; and bottom rows, 1:2. Images in the left column are identical MRA created from a 100% sampling rate (1.0X or MRA-full). Images in the second left column are ZF-MRA, and images in the middle to the right columns are CS-MRA with 5, 10, or 50 iterations, respectively. The best CS parameter set for each sampling density led to images nearly equal to the chosen image.

Supplemental Digital Content 4

The size, neck, height, and aspect ratio (height / neck) of CS 8.0X (5, 10, 50 iteration) and CS 5.0X (5, 10, 50 iteration) were measured by two observers. The measured results were shown (4A, 4B, 4C, 4D, 4E and 4F, respectively).

Supplemental Digital Content 5

The intraclass correlation coefficient (ICC) of measured size, neck, height and aspect ratio between observer 1 and observer 2 were calculated.

List of Supplemental Digital Content

Supplemental_1_Table.docx

Supplemental_2a_Source_Acom_Aneurysm.tif

Supplemental_2b_MIP_Acom_Aneurysm

Supplemental_3a_Source_RightMCA_Aneurysm.TIF

Supplemental_3b_MIP_RightMCA_Aneurysm.TIF

Supplemental_4A_Table CS8.0X_05iter.docx

Supplemental_4B_Table CS8.0X_10iter.docx

Supplemental_4C_Table CS8.0X_50iter.docx

Supplemental_4D_Table CS5.0X_05iter.docx

Supplemental_4E_Table CS5.0X_10iter.docx

Supplemental_4F_Table CS5.0X_50iter.docx

Supplemental_5_ICC.docx

Supplemental Digital Content 1

Sampling Rate	Central Low Frequency Part (mm)	Sampling Density Ratio between High and Moderate Frequency Part	μ	ε	δ	λ1 - λ2 - λ3	Iteration	Outer Loop
8.0×	60 (Medium)	2 : 1	10^{-8}	10^{-1} or 10^{-2} or 10^{-3}	10^{-1} or 10^{-2} or 10^{-3} or 10^{-4} or 10^{-8} or 10^{-12} or 10^{16}	0 - 1 - 0	50	1
8.0×	48 (Small)	1 : 1	10^{-8}	10^{-4}	10^{-4} or 10^{-8} or 10^{-12} or 10^{16}	0 - 1 - 0	50	1
8.0×	48 (Small)	1 : 2	10^{-8}	10^{-4}	10^{-4} or 10^{-8} or 10^{-12} or 10^{16}	0 - 1 - 0	50	1
5.0×	60 (Medium)	2 : 1	10^{-4}	10^{-8} or 10^{-12}	10^{-4} or 10^{-8} or 10^{-12} or 10^{16}	0 - 0 - 1	50	2
5.0×	48 (Small)	1 : 1	10^{-4}	10^{-12}	10^{-4} or 10^{-8} or 10^{-12} or 10^{16}	0 - 0 - 1	50	1
5.0×	48 (Small)	1 : 2	10^{-8}	10^{-4}	10^{-4} or 10^{-8} or 10^{-12} or 10^{16}	0 - 1 - 0	50	1

Supplemental Digital Content 2A

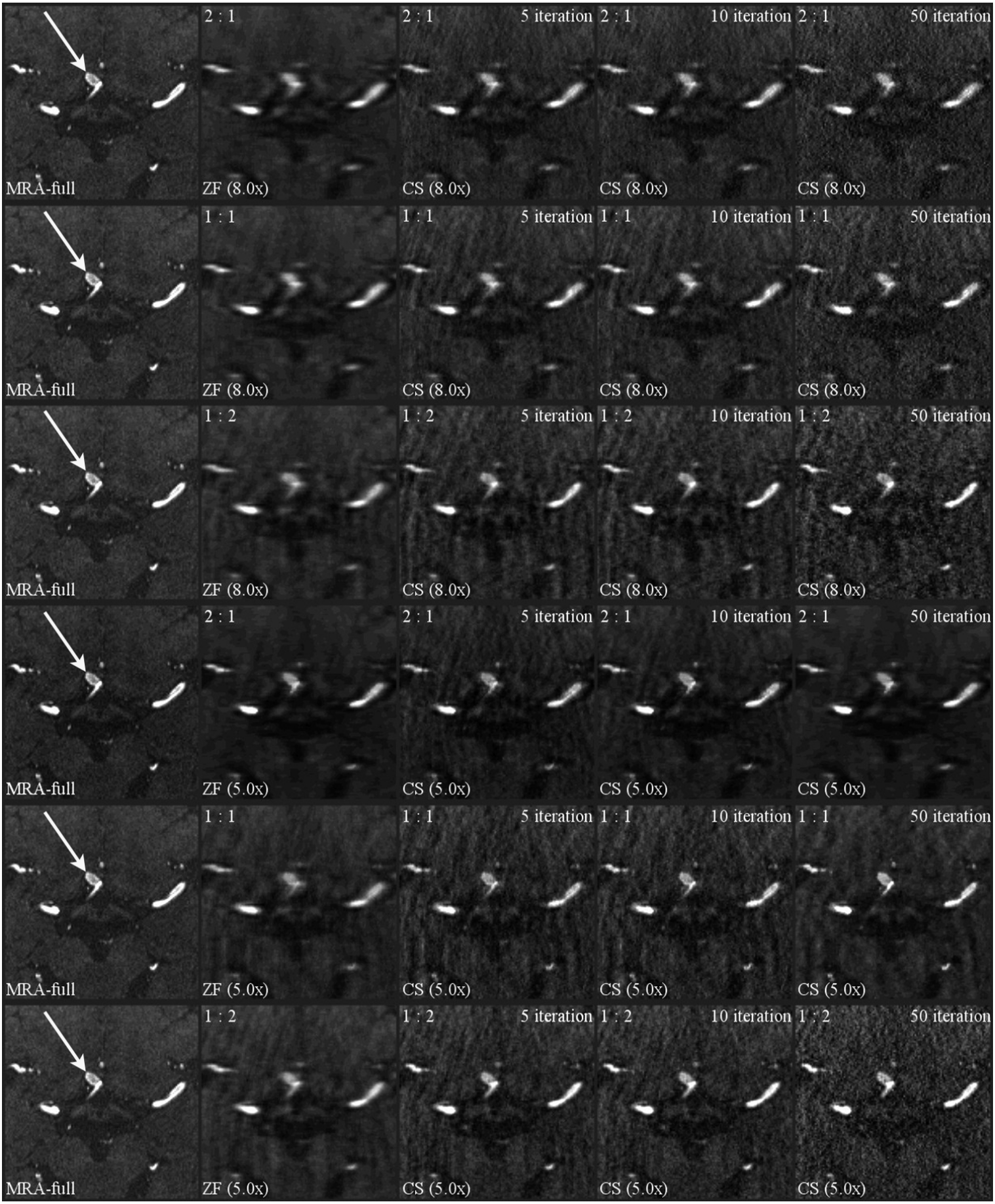

Supplemental Digital Content 2B

Supplemental Digital Content 3A

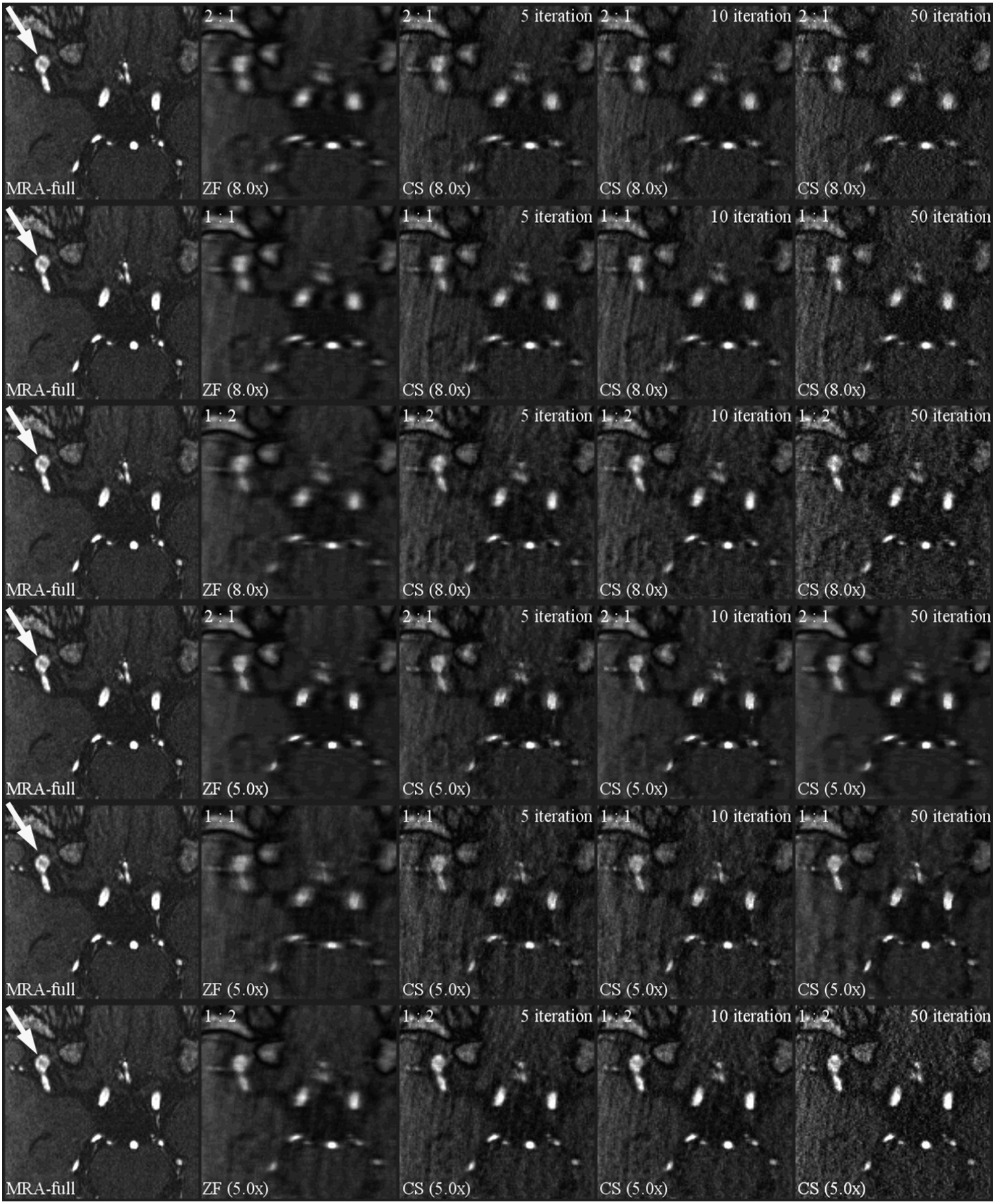

Supplemental Digital Content 3B

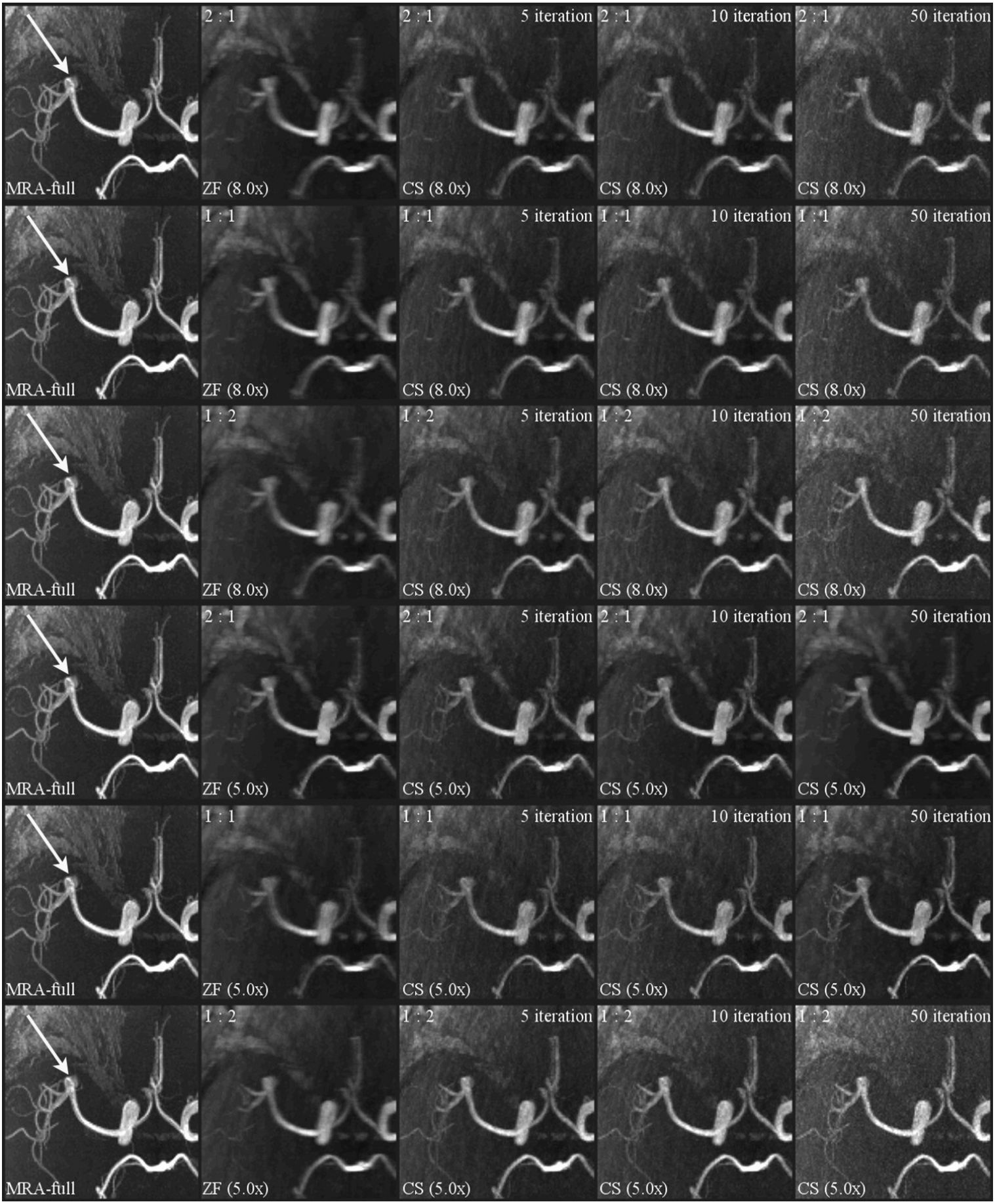

Supplemental Digital Content 4A

CS 8.0X 5 iteration

	Observer 1				Observer 2			
	Size	Neck	Height	Aspect Ratio	Size	Neck	Height	Aspect Ratio
Case 1	6.29	2.63	5.44	2.06	4.84	3.55	4.84	1.36
Case 1	2.22	1.45	2.22	1.53	2.29	1.72	2.29	1.33
Case 2	8.83	8.42	5.26	0.63	8.75	7.74	6.78	0.88
Case 3	5.76	3.60	4.10	1.14	6.45	4.14	5.81	1.40
Case 4	6.18	2.35	3.71	1.58	4.90	3.23	5.94	1.84
Case 5	8.24	4.43	6.34	1.43	7.96	3.95	8.21	2.08
Case 6	6.51	1.88	6.51	3.47	6.38	1.86	6.38	3.43
Case 7	3.48	2.23	2.83	1.27	2.85	1.72	3.79	2.21
Case 8	5.90	3.67	5.52	1.51	4.89	3.45	4.89	1.42
Case 9	5.37	1.62	5.37	3.31	6.51	1.82	6.51	3.57
Case 10	5.02	3.33	4.39	1.32	5.04	2.84	5.04	1.77

Supplemental Digital Content 4B

CS 8.0X 10 iteration

	Observer 1				Observer 2			
	Size	Neck	Height	Aspect Ratio	Size	Neck	Height	Aspect Ratio
Case 1	6.45	2.49	5.42	2.17	4.79	2.83	4.79	1.69
Case 1	2.22	1.41	2.22	1.58	2.28	1.68	2.28	1.36
Case 2	8.79	8.34	5.25	0.63	8.73	7.42	6.37	0.86
Case 3	5.60	3.66	4.10	1.12	6.23	3.89	5.79	1.49
Case 4	6.14	2.31	3.77	1.63	4.96	3.17	5.98	1.89
Case 5	8.17	4.38	6.18	1.41	7.90	3.88	8.20	2.11
Case 6	6.48	1.82	6.48	3.56	6.42	1.82	6.42	3.53
Case 7	3.45	2.16	2.78	1.29	2.85	1.70	3.42	2.01
Case 8	5.86	3.63	5.51	1.52	4.89	3.39	4.89	1.45
Case 9	5.47	1.55	5.47	3.53	6.35	1.74	6.35	3.64
Case 10	5.04	2.94	4.32	1.47	4.96	2.78	4.96	1.78

Supplemental Digital Content 4C

CS 8.0X 50 iteration

	Observer 1				Observer 2			
	Size	Neck	Height	Aspect Ratio	Size	Neck	Height	Aspect Ratio
Case 1	6.31	2.50	5.41	2.16	4.64	3.18	4.64	1.46
Case 1	2.36	1.32	2.36	1.79	2.38	1.67	2.38	1.42
Case 2	8.65	8.25	5.23	0.63	8.69	7.44	6.32	0.85
Case 3	5.26	3.73	4.05	1.09	5.97	4.09	5.74	1.40
Case 4	6.23	2.17	3.96	1.82	5.38	3.11	5.87	1.89
Case 5	8.03	4.20	5.56	1.32	7.75	3.61	8.06	2.23
Case 6	6.42	1.76	6.42	3.65	6.41	1.77	6.41	3.62
Case 7	3.40	2.05	2.67	1.30	2.83	1.60	3.30	2.06
Case 8	5.44	3.50	5.44	1.55	4.90	3.22	4.90	1.52
Case 9	5.23	1.47	5.23	3.56	6.45	1.81	6.45	3.57
Case 10	6.03	2.65	4.17	1.58	4.75	2.91	4.61	1.58

Supplemental Digital Content 4D

CS 5.0X 5 iteration

	Observer 1				Observer 2			
	Size	Neck	Height	Aspect Ratio	Size	Neck	Height	Aspect Ratio
Case 1	5.43	2.64	5.22	1.98	4.89	3.47	4.89	1.41
Case 1	2.42	1.38	2.42	1.75	2.39	1.57	2.39	1.52
Case 2	8.61	8.50	5.27	0.62	8.52	7.40	6.49	0.88
Case 3	6.42	3.92	3.76	0.96	6.80	4.76	5.42	1.14
Case 4	5.84	2.82	3.91	1.39	5.32	3.06	5.82	1.90
Case 5	7.76	4.32	6.13	1.42	8.00	3.87	8.28	2.14
Case 6	6.37	1.82	6.37	3.50	6.34	1.82	6.34	3.48
Case 7	3.45	1.99	2.70	1.36	2.95	1.72	3.51	2.04
Case 8	5.08	3.79	5.08	1.34	4.90	3.48	4.90	1.41
Case 9	5.88	1.64	5.55	3.38	6.49	1.91	6.49	3.40
Case 10	6.08	2.78	4.15	1.49	4.86	3.06	4.78	1.56

Supplemental Digital Content 4E

CS 5.0X 10 iteration

	Observer 1				Observer 2			
	Size	Neck	Height	Aspect Ratio	Size	Neck	Height	Aspect Ratio
Case 1	5.38	2.64	5.18	1.96	4.89	3.45	4.89	1.42
Case 1	2.37	1.34	2.37	1.76	2.36	1.57	2.36	1.50
Case 2	8.55	8.32	5.27	0.63	8.64	7.40	6.48	0.88
Case 3	6.24	3.90	3.76	0.97	6.80	4.39	5.49	1.25
Case 4	5.80	2.73	3.94	1.44	5.31	3.09	5.81	1.88
Case 5	7.76	4.21	6.02	1.43	7.96	3.83	8.30	2.17
Case 6	6.36	1.80	6.36	3.53	6.31	1.79	6.31	3.53
Case 7	3.40	1.92	2.60	1.35	2.94	1.72	3.50	2.04
Case 8	5.12	3.69	5.12	1.39	5.00	3.41	5.00	1.46
Case 9	5.83	1.63	5.53	3.39	6.32	1.89	6.32	3.34
Case 10	5.28	2.75	4.14	1.51	4.92	3.15	4.76	1.51

Supplemental Digital Content 4F

CS 5.0X 50 iteration

	Observer 1				Observer 2			
	Size	Neck	Height	Aspect Ratio	Size	Neck	Height	Aspect Ratio
Case 1	5.20	2.62	5.16	1.97	4.84	3.47	4.84	1.39
Case 1	2.32	1.22	2.32	1.90	2.24	1.53	2.24	1.46
Case 2	8.39	7.98	5.32	0.67	8.55	7.42	6.41	0.86
Case 3	6.60	3.89	3.77	0.97	6.38	4.84	5.44	1.12
Case 4	5.65	2.63	3.97	1.51	5.42	3.23	5.84	1.80
Case 5	7.78	4.21	5.96	1.42	8.06	3.63	8.30	2.28
Case 6	6.32	1.78	6.32	3.56	6.19	1.66	6.19	3.73
Case 7	3.28	1.80	2.44	1.36	2.96	1.59	3.47	2.18
Case 8	5.19	3.52	5.19	1.48	5.15	3.27	5.15	1.57
Case 9	5.88	1.54	5.50	3.57	6.31	2.00	6.31	3.15
Case 10	5.23	2.71	4.12	1.52	5.07	3.36	4.98	1.48

Supplemental Digital Content 5

Intraclass Correlation Coefficient between Observer 1 and Observer 2.

	Size	Neck	Height	Aspect Ratio
CS 8X 5 iteration	0.9125	0.9567	0.6874	0.8629
CS 8X 10 iteration	0.9155	0.9668	0.7112	0.9079
CS 8X 50 iteration	0.8956	0.9578	0.6651	0.8822
CS 5X 5 iteration	0.9599	0.9574	0.724	0.8991
CS 5X 10 iteration	0.9802	0.9668	0.7165	0.8983
CS 5X 50 iteration	0.9908	0.9519	0.7142	0.8718